

Similar but Different: Structural and Spectroscopic Characterization of Series of Neodymium, Europium, Americium, and Curium Coordination Complexes

Ian Colliard* and Gauthier J.-P. Deblonde*



Cite This: <https://doi.org/10.1021/jacs.5c00861>



Read Online

ACCESS |

Metrics & More

Article Recommendations

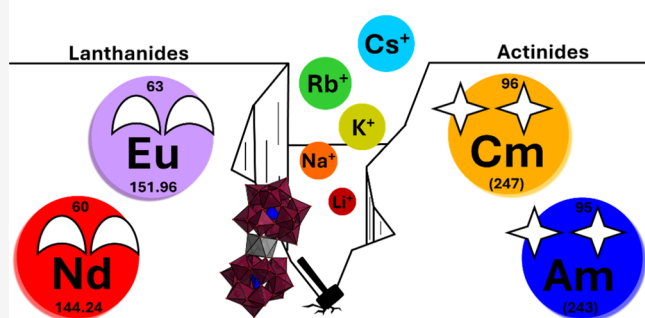
Supporting Information

ABSTRACT: Series of curium, americium, europium, and neodymium complexes with five different polyoxometalate (POM) ligands were structurally and spectroscopically characterized: $\text{Na}_x\text{Cs}_y[\text{M}(\text{XW}_{11}\text{O}_{39})_2] \cdot n\text{H}_2\text{O}$, where $\text{M} = \text{Nd}^{3+}$, Eu^{3+} , Am^{3+} , or Cm^{3+} and $\text{X} = \text{B}^{3+}$, Ga^{3+} , Si^{4+} , Ge^{4+} , or P^{5+} . This first “serial approach” on transplutonium chemistry was allowed by minimizing the amount of f-element needed per synthesis down to $\sim 10 \mu\text{g}$. This offers a unique opportunity to contrast structural and spectroscopic properties of trivalent actinide with those of lanthanide compounds under identical conditions. The results showcase that although actinide(III) and lanthanide(III) can make isostructural complexes, their solid-state coordination chemistries deviate significantly. The curium and americium compounds were found to be more uniform than their europium and neodymium counterparts, respectively. The particular symmetry of the Cm-POMs also enables the observation of rarely seen emission bands, which hints at vibronic coupling or new emissive pathways. Additionally, the Cm-POM and Eu-POM complexes were characterized via steady-state and time-resolved excitation and emission spectroscopy in solutions containing five different counterions (Li^+ , Na^+ , K^+ , Rb^+ , or Cs^+), representing 50 combinations of alkali/[$\text{M}^{III}(\text{XW}_{11})_2$] $^{n-}$ complexes. The Cm-POMs respond to the alkali counterions by improving symmetry from Li^+ to Cs^+ , while the Eu-POMs do the opposite. The luminescence lifetimes of the Cm-POMs also depart from the ideal Kimura equation. This study provides a rare, and perhaps the most comprehensive, experimental data set comparing heavy actinides and lanthanides via single crystal XRD plus, solution-state, solid-state, and time-resolved emission spectroscopy and demonstrates that lanthanides are only a coarse approximation for actinide elements.

INTRODUCTION

The periodic table of elements, as we currently know it, has a rich history rooted in attempts to understand the fundamental building blocks of matter.¹ Its ability to predict the characteristics of missing elements has been instrumental in the quest for isolating and characterizing new elements, and this quest is still ongoing today, with the potential opening of a new periodic row once or if element 120 is synthesized and the prediction of an island of stability with relatively stable (but still radioactive) isotopes beyond $Z \geq 120$.^{2–4} In a contemporary context, the most recent systemic change to the periodic table happened with the synthesis of elements beyond the natural ones, i.e., the transuranic actinides ($Z > 92$), by Seaborg and colleagues throughout the 1940s (Np , Pu , Am , Cm , Bk), 1950s (Cf , Es , Fm , Md , No), and 1960s (Lr).^{5–8} Since then, the actinide series ($Z = 89$ to 103) has been placed below the lanthanide series ($Z = 57$ to 71). From a nuclear property standpoint, the 15 elements of the actinide series are all radioactive, and their isotope stability generally decreases from U to Lr . As such, the predictive capability of the periodic table is often conveniently invoked to

Differentiating Physiochemical Properties



approximate the behavior of transuranic actinides with that of the lanthanides. In particular, the similar electronic structure, ionic radius, and physiochemical behavior have made the lanthanides the go-to proxies for studying the trivalent actinides (e.g., Pu^{3+} , Am^{3+} , Cm^{3+} ...).

Nonetheless, due to the radioactive nature, rarity, and high cost of research isotopes of transplutonium elements, experimental comparisons between actinides and lanthanides have been limited to seldom examples. In fact, when compared to other elements, only a very small number of transplutonium coordination compounds have been synthesized and characterized via single crystal X-ray diffraction and optical spectroscopies. Breakthrough studies have yielded the first Cf^{3+}

Received: January 17, 2025

Revised: April 1, 2025

Accepted: April 3, 2025

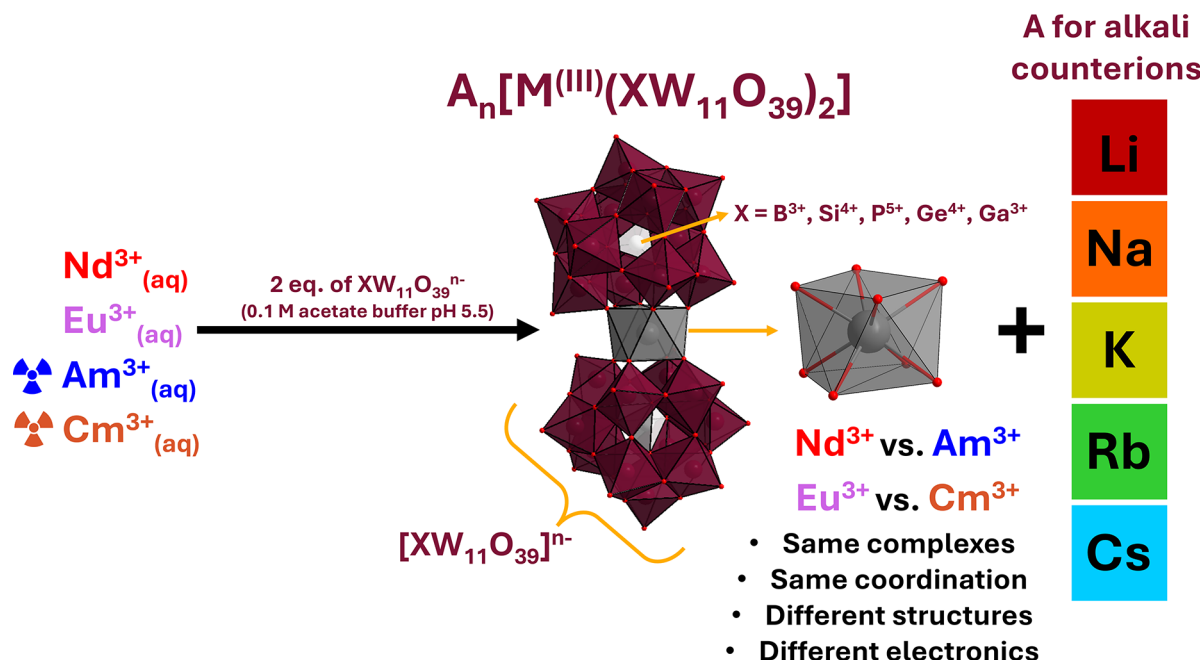


Figure 1. Simplified version of the f-element/POM complex synthesis scheme. Nd^{3+} , Eu^{3+} , Am^{3+} , and Cm^{3+} can react with two POM ligands, $[XW_{11}O_{39}]^{n-}$, resulting in an 8-coordinated central cation. The complexes for both europium and curium exhibit the same general speciation (metal:POM ratio of 1:2, formula $A_x[M(XW_{11}O_{39})_2]\cdot nH_2O$) but we can change the counterion ion and directly or indirectly probe the effects on the f-element⁺ through crystallography and luminescence spectroscopy for Eu^{3+} and Cm^{3+} as both exhibit luminescence emission in the visible range. A = alkali ion (Li^+ , Na^+ , K^+ , Rb^+ , or Cs^+). X = heteroelement within the POM (B^{3+} , Si^{4+} , P^{5+} , Ge^{4+} , or Ga^{3+}).

compound in 2005 (iodate complex),⁹ and then a few more (with dipicolinate,¹⁰ borate,¹⁰ dioxophenoxazine,¹¹ dithiocarbamate,¹² mellitate,^{13,14} terpyridyl,¹⁵ metallocene,¹⁶ and squareoxalate¹⁷ ligands). The first and so far the only Cf^{2+} compound was reported in 2023 (crown ether ligand),¹⁸ while the first Bk^{3+} was isolated in 2016, and the first Am^{4+} and Bk^{4+} in 2009¹⁹ and 2017,²⁰ respectively. The first single crystal structure of an americyl (AmO_2^{2+}) compound was reported in 2023.²¹ Am^{3+} and Cm^{3+} complexes have been synthesized and structurally characterized with the same or similar ligands at a pace of about one per year.^{22–27} These compounds were all obtained from ~ 5 mg scale syntheses, which has limited the scope of these studies. Indeed, synthesizing and obtaining single crystals for transplutonium compounds is inherently limited by the low isotope quantities available to chemists (a few milligrams, at best), which has prevented the obtention of analogous series of lanthanide versus actinide compounds.

Herein, we took on the challenge of advancing transplutonium element chemistry, with the goal of obtaining consistent crystallographic and spectroscopic data sets of compounds of this truly rare element. We synthesized a series of coordination complexes of Am^{3+} and Cm^{3+} with five different polyoxometalate (POM) ligands: $HBW_{11}O_{39}^{8-}$, $PW_{11}O_{39}^{7-}$, $SiW_{11}O_{39}^{8-}$, $GeW_{11}O_{39}^{8-}$, and $GaW_{11}O_{39}^{9-}$ (Abbreviated “ XW_{11} ”). This effort led to a total of seven different single crystal structures for curium and six for americium, representing a significant increase in the number of known compounds for this element. The series also includes the first curium compounds with ligands containing silicon, germanium, and gallium. All compounds were characterized via single crystal XRD. The Cm -POMs were also characterized via solution-state and solid-state excitation and emission spectroscopy. This study was enabled by leveraging a microgram-scale synthetic protocol.²⁸ The analogous Nd^{3+} (lanthanide size-match for

Am^{3+}) and Eu^{3+} (relatively good size-match and fluorescence analogue for Cm^{3+}) were also synthesized and characterized (Table S2). While europium and neodymium are not particularly rare, the lanthanide and actinide series of $[M^{III}(XW_{11})_2]^{n-}$ ($M = Nd^{3+}$, Eu^{3+} , Am^{3+} or Cm^{3+} ; $X = B^{3+}$, P^{4+} , Si^{4+} , Ge^{4+} , or Ga^{3+}) complexes were synthesized via the same microgram synthesis approach to maintain comparability across the complexes and their lattices. To the best of our knowledge, this represents the largest crystallographic data set comparing heavy actinides and lanthanides.

The results showcase that, although Nd^{3+} vs Am^{3+} and Eu^{3+} vs Cm^{3+} can make isostructural complexes, their solid-state coordination chemistries deviate significantly. Furthermore, the luminescent characteristics of Eu-POMs and Cm-POMs in solution were observed to be impacted by the alkali counterions—even though they are typically considered as spectator ions. The Cm-POM and Eu-POM complexes with the five different POMs were all characterized in solutions containing five different counterions (Li^+ , Na^+ , K^+ , Rb^+ , or Cs^+), representing 25 combinations of the alkali/[$M^{III}(XW_{11})_2]^{n-}$ complex for both curium and europium. The solid-state luminescence spectra for single crystals of the five Cm-POMs and five Eu-POMs (with a Cs^+ counterion) were also measured. This represents one of the most exhaustive luminescence spectroscopy data sets comparing curium and a lanthanide. Diverging spectroscopic properties were observed for Eu^{3+} and Cm^{3+} as functions of the alkali counterion. The origin of the diverging behavior for Eu^{3+} and Cm^{3+} seems to stem from the site symmetry of the f-element, which reacts differently with the different counterions, thus yielding 4f- versus 5f-specific luminescing behaviors.

RESULTS

We briefly summarize the synthesis for all structures here: POM complexes were formed *in situ* in aqueous solution at pH 5.5. The metal-POM solution is made by diluting stock solutions of the lanthanide or actinide trichloride at stoichiometric amounts (metal:POM ratio of 1:2); refer to the SI for more details. For crystallization, excess Cs⁺ is added (>6 M CsCl) to a 100 μM metal-POM solution. The quantity of f-elements (i.e., Nd³⁺, Eu³⁺, ²⁴³Am³⁺, or ^{248/246}Cm³⁺) engaged in these reactions was only 12 μg for the actinides and 8 μg for the lanthanides. This represents an isotope consumption ~500 times lower than for traditional ~5 mg-scale syntheses done for transuranic elements (and more for lanthanide syntheses, typically done at the gram-scale). As we previously demonstrated,^{28–30} the use of heavy POMs, like the polyoxotungstates studied here, allows for the crystallization of their complexes at the microscale, which unlocks the experimental investigation of americium and curium chemistry in a series of compounds rather than one at a time. While lanthanides are not particularly rare elements, and experiments could have been done at a much larger scale, we also crystallized the Eu-POM and Nd-POM complexes at the microscale for a consistent comparison. This limits any potential scale effect that may arise when comparing rare compounds synthesized in minute quantities to more common materials synthesized in bulk.

Single crystals large enough for X-ray diffraction were harvested and obtained within a few days of the crystallization tests. The structures reported herein are all hydrates and isotopic, with the same general formula of Na_xCs_yH_z[M-(XW₁₁O₃₉)₂]·nH₂O, where M = Nd³⁺, Eu³⁺, Am³⁺, or Cm³⁺ (Figure 1). Only BW₁₁ is protonated under these conditions, HBW₁₁O₃₉⁸⁻, consistent with the structure of the uncomplexed POM previously reported by Téze et al.³¹ The Keggin ligands used for this study are considered lacunary derivatives of the plenary structure α-XW₁₂O₄₀ⁿ⁻.³² The plenary structure is composed of 12 octahedral [WO₆] units grouped into four trimer sets, with each trimer connected to central heteroelements [XO₄] with overall tetrahedral symmetry.³³ These lacunary Keggin POMs then act as tetradeinate ligand, α-XW₁₁O₃₉ⁿ⁻, where two POM anions can bind to Ln³⁺, An³⁺, or almost any other cation and can be crystallized in the presence of alkali ions.³⁴ The central metal cation is surrounded by oxygens from the two tetradeinate POM ligands coming from opposite directions and, thus, bound in an eight-coordinate environment, typically with square antiprismatic geometry (Figure 1). Twelve new single crystal structures were obtained (two with Nd³⁺, three with Eu³⁺, four with Am³⁺, and three with Cm³⁺) and, when combined with structures that we recently reported in separate studies,^{28,29} they represent a complete series of curium, americium, neodymium, and europium coordination compounds with the five different Keggin ligands HBW₁₁O₃₉⁸⁻, PW₁₁O₃₉⁷⁻, SiW₁₁O₃₉⁸⁻, GeW₁₁O₃₉⁸⁻, and GaW₁₁O₃₉⁹⁻ (see Table S2 for the full formula and CCDC deposition numbers). We note that, under the same conditions, Cm³⁺ led to seven different structures with five POMs, whereas Am³⁺, Nd³⁺, and Eu³⁺ led to six different structures (see Table S1 for notations and Table S2 for the list of structures).

For the new Eu³⁺ compounds reported here, Eu(SiW₁₁)₂-Cs is fully formulated as Cs₁₃Eu(SiW₁₁O₃₉)₂·21H₂O and crystallizes in the anorthic space group P-1 with a cell volume of 5452.36(16) Å³. Eu(GeW₁₁)₂-Cs is fully formulated as Cs₁₃Eu(GeW₁₁O₃₉)₂·13H₂O and crystallizes in monoclinic space group

P2₁/n with a cell volume of 9829.5(3) Å³. Eu(GaW₁₁)₂-Cs is fully formulated as Na₃Cs₁₂Eu(GaW₁₁O₃₉)₂·5H₂O and crystallizes in monoclinic space group P2₁/c with a cell volume of 10038.1(10) Å³. Table S3 gives detailed crystallographic information about each Eu³⁺ crystal structure. Table S5 gives detailed crystallographic information for the Nd³⁺ crystal structure. Additional information on structural parameters and descriptions of the structures are shown in Figures S1–S3. For information about the solvent mask used for both lanthanides and actinides, see Table S7.

For the new Cm³⁺ compounds reported here, Cm(SiW₁₁)₂-Cs is fully formulated as Cs₁₃Cm(SiW₁₁O₃₉)₂·13H₂O and crystallizes in the monoclinic space group P2₁/n with a cell volume of 9888.9(3) Å³. Cm(GeW₁₁)₂-Cs is fully formulated as Cs₁₃Cm(GeW₁₁O₃₉)₂·15H₂O and crystallizes in the monoclinic space group P2₁/n with a cell volume of 9826.4(3) Å³. Cm(GaW₁₁)₂-Cs is fully formulated as Na₃Cs₁₂Cm(GaW₁₁O₃₉)₂·2.75H₂O and crystallizes in monoclinic space group P2₁/n with a cell volume of 9866.0(4) Å³. Table S4 gives detailed crystallographic information about the Cm³⁺ crystal structures. Additional Raman spectra on Cm³⁺ structures are available in Figure S5.

For the new Am³⁺ compounds reported here, Am(BW₁₁)₂-Cs is fully formulated as Cs₁₃Am(HBW₁₁O₃₉)₂·14.5H₂O and crystallizes in the monoclinic space group P2₁/n with a cell volume of 9645.0(5) Å³. Am(SiW₁₁)₂-Cs is fully formulated as Cs₁₃Am(SiW₁₁O₃₉)₂·17H₂O and crystallizes in the monoclinic space group P2₁/n with a cell volume of 9775.8(3) Å³. Am(GeW₁₁)₂-Cs is fully formulated as Cs₁₃Am(GeW₁₁O₃₉)₂·14H₂O and crystallizes in the monoclinic space group P2₁/n with a cell volume of 9764.3(2) Å³. Am(GaW₁₁)₂-Cs is fully formulated as NaCs₁₄Am(GaW₁₁O₃₉)₂·21H₂O and crystallizes in the monoclinic space group P2₁/n with a cell volume of 9758.6(4) Å³. Table S6 gives detailed crystallographic information about each Am³⁺ crystal structure.

We have previously defined select structural parameters to describe the properties of these seemingly simple complexes.³⁴ Five structural parameters were established: (1) the average bond length of the complexed metal, here Nd³⁺, Eu³⁺, Am³⁺, or Cm³⁺, abbreviated as BL(M³⁺); (2) the distance between the two encapsulated [XO₄]ⁿ⁻ anions, previously labeled as d(X-X), herein abbreviated by δ (unit: Å); (3) the bending angle of the complex with respect to the central M³⁺, <(X-M-X), herein denoted through θ (unit: °); (4) the torsion angle between the dihedral planes of the encapsulated [XO₄]ⁿ⁻, <(X-M-X), herein denoted by ϕ (unit: °). Since there are two possible binding configurations at 45 and 135° (Figure S1), the torsion is taken as the absolute value of the angle between the ideal sites. The θ and ϕ angles can be used to describe the distortion from the ideal D_{4d} symmetry for the central cation. Lastly, the fifth parameter is the number of Cs⁺ cations 4.5–5 Å away from the central M, here within the range denoted by ξ. These counterions are found in the equatorial plane of the complex and are thought to influence the properties of the central metal.³⁰ A full list of abbreviations is available in Table S1, and all structural parameters are listed in Table S8.

We summarize here the trends observed for the Eu-POM versus Cm-POM crystal structures. Similar observations can be made for the Nd-POM versus Am-POM structures. For Eu(XW₁₁)₂ (X = B, P, Si, Ge, and Ga), we observe that δ ranges from 9.316 to 8.800 Å. The bending angle range is θ = 159.668–166.361°, except for GeW₁₁ which stands out with a θ of 178.295°. We observe a similar pattern with the twisting angle, ϕ = 8.378 to 13.082°, whereas GeW₁₁ is an outlier with a

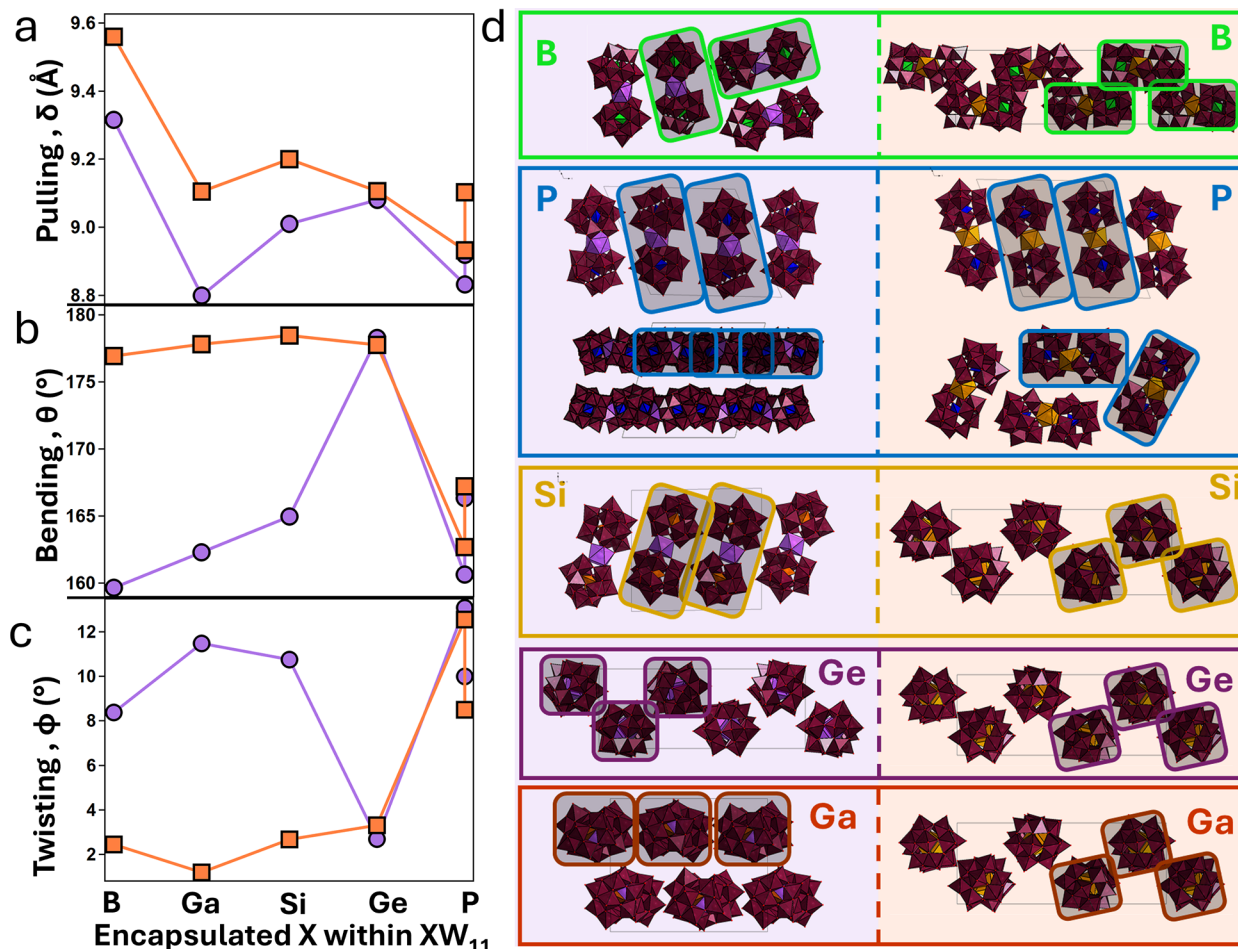


Figure 2. Structural effects in the curium and europium POM complexes as a function of the heteroelement (ranked by charge and then atomic number: B³⁺, Ga³⁺, Si⁴⁺, Ge⁴⁺, and P⁵⁺). (a) Pulling, (b) bending, and (c) twisting. See Figure S1 for a detailed schematic alongside polyhedral representations of the unit cell view along the (100) axis. (d) Comparison of Eu(XW₁₁)₂ vs Cm(XW₁₁)₂ structures (X = B, P, Si, Ge, and Ga). Colored boxes are overlaid to illustrate the orientation of the complexes. Color code: W is colored maroon, Eu light purple, Cm orange, B green, P blue, Si yellow, Ge pink, Ga brown, and oxygen in red. Counterions and water molecules have been omitted for the sake of clarity. All compounds follow the general formula: Na_xCs_yH_z[M(XW₁₁O₃₉)_n]_nH₂O. Note that the α isomer of PW₁₁ yields two different structures with Eu³⁺ and Cm³⁺, as we recently reported (Table S2).^{29,28} See Table S1 for definitions of the pulling, bending, and twisting parameters in these structures.

much smaller ϕ of 2.708°. In other words, Eu(GeW₁₁)₂ is the Eu-POM complex closest to the ideal geometry (least bending and twisting). As for the number of equatorial Cs⁺, ξ ranges from 2 to 4 Cs⁺, with GeW₁₁ having the lowest (ξ = 2) and SiW₁₁ having the highest (ξ = 4).

The Cm(XW₁₁)₂ structures, on the other hand, have somewhat opposite behavior. We observe δ ranging from 9.106 to 8.909 Å. The bending angle range is θ = 176.946–178.462°, except for PW₁₁ as an outlier (θ = 162.709 to 167.227°; three structures). The twisting effect is smaller for Cm, with ϕ = 1.205–3.319°, with PW₁₁ still an outlier, with a much larger ϕ of 8.510 and 13.611° (note that we obtained three different structures for Cm(PW₁₁)₂, with two containing the α isomer of PW₁₁ and one with the β isomer). As for the number of equatorial Cs⁺, ξ ranges from 1 to 3 Cs⁺, with GeW₁₁ having the lowest ξ = 1.

We previously established the affine relationship between the size of the central metal and its corresponding bond lengths for XW₁₁ with a series of metals ranging from the small Ce⁴⁺ to the large Ba²⁺.³⁴ However, the remaining structural parameters defined above (δ , θ , ϕ , and ξ) do not necessarily follow the same simple correlation. The vast structural diversity in these POM

complexes is manifested well beyond the first coordination sphere of the central cation. As shown in Figure 2a–c, the pulling, bending, and twisting (δ , θ , ϕ) of the POM ligands, relative to the central metal, were found to vary depending on both the encapsulated heteroelement and the central cation, with europium and curium having distinct trends.

Furthermore, the cesium counterions were determined to be direct participants within the complex, yielding very different structural arrangements of the complexes in forming crystals (Figures 2d and 4, and Figure S2). The complexes display varying propensities to bind tightly to 1 to 5 Cs⁺, which can correlate to the other structural parameters, which in turn affects the lattice arrangement. These equatorial Cs⁺ ions bind directly to the square antiprism geometry of the captured metal (Figure 4). Between the Eu³⁺ and the Cm³⁺ structures, only GeW₁₁ and one of the PW₁₁ polymorphs share a similar arrangement of the complexes (Figure 2d). Interestingly, the Eu³⁺ structures feature a wider variety of arrangements compared to Cm³⁺, and out of the six structures, there are five different arrangements for the complexes. Cm³⁺, on the other hand, features some uniformity, where out of the seven structures, there are four arrangement

types, and the structures with GeW_{11} , SiW_{11} , and GaW_{11} are similar.

DISCUSSION

Overall Structural Effects in Eu and Cm Complexes with XW_{11} Ligands ($\text{X} = \text{B}, \text{P}, \text{Si}, \text{Ge}$, and P). Previously, only the PW_{11} analogs for $\text{Am}(\text{XW}_{11})_2$ $\text{Cm}(\text{XW}_{11})_2$ and $\text{Ln}(\text{XW}_{11})_2$ had been compared,²⁸ where therein, the conclusion was that americium and curium do not fit with the general structural trends that were predicted from the lanthanide series of $\text{Cs-Ln}(\text{PW}_{11})_2$ complexes ($\text{Ln} = \text{La}^{3+}$ to Lu^{3+}). The broader context provided here with the five different XW_{11} POMs reinforces and expands these observations. In fact, some of the analogous $\text{Ln}(\text{XW}_{11})_2$ and $\text{An}(\text{XW}_{11})_2$ compounds reported here diverge even more than the first case we were able to synthesize (PW_{11}).²⁸ For the sake of conciseness, hereafter, we discuss in detail the Eu^{3+} versus Cm^{3+} structures, but the conclusions are further corroborated when comparing the Nd^{3+} versus Am^{3+} structures. Figure 2a–c showcases the pulling, bending, and twisting effects for both Eu^{3+} and Cm^{3+} as a function of the heteroelements in XW_{11} . Figure 3 gives an overview of the structural differences with An^{3+} -POMs and Ln^{3+} -POMs, as detailed below.

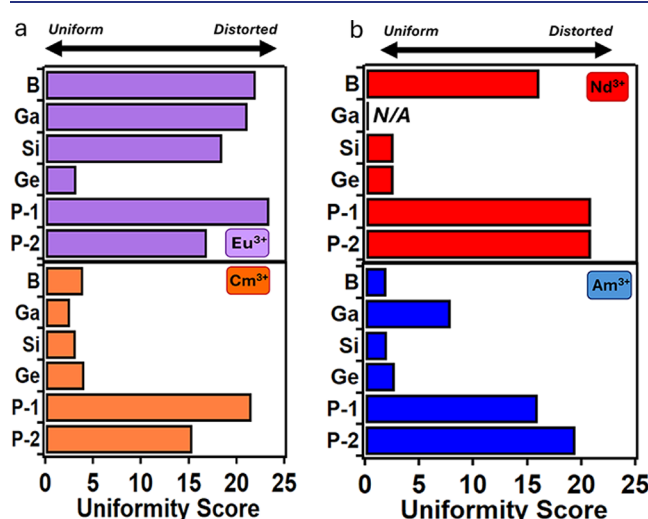


Figure 3. Uniformity/distortion score for the series of (a) Eu^{3+} versus Cm^{3+} , and (b) Nd^{3+} versus Am^{3+} complexes with the POMs $\text{XW}_{11}\text{O}_{39}^{n-}$ ($\text{X} = \text{B}^{3+}, \text{Ga}^{3+}, \text{Si}^{4+}, \text{Ge}^{4+}$, or P^{5+}). Note that the score tends to be higher for Eu^{3+} versus Cm^{3+} , or for Nd^{3+} versus Am^{3+} . The uniformity/distortion score is defined as follows: the higher the score the more distorted the complex. A score of zero corresponds to ideal D_{4d} symmetry. No structure was obtained or has been reported for Nd^{3+} with GaW_{11} . The results shown here are further corroborated with evaluation of the compounds' point group symmetry by the CSOM computer code³⁵ (see Figure S4).

Although there are some exceptions, several patterns based on the structural parameters emerge for the series of structures. First, the BW_{11} ligand yields stretched complexes (longer δ , Figure 2a), whereas the other four XW_{11} have shorter complexes. Second, Cm^{3+} generally has a smaller ξ value, or number of active Cs^+ , see Figure S2 and Table S8. Third, bending and twisting effects work in tandem; the more the complex bends, the more it twists. As directly seen in Figure 2b,c, the trends for these two parameters are highly correlated. This was quantified by calculating the statistical Pearson's correlation coefficient

between θ and ϕ , which revealed a nearly perfect negative linear relationship, -0.84 and -0.98 respectively (Figure S3). Since the ideal complex geometry would not display any bending and twisting ($\theta_{\text{ideal}} = 180^\circ$ and $\phi_{\text{ideal}} = 0^\circ$), we can additionally calculate a ‘uniformity score’ to determine which complex deviates the most from the ideal geometry. We define this score by eq 1, and it is plotted in Figure 3a for the two series of Cm^{3+} and Eu^{3+} complexes and Figure 3b for the two series of Am^{3+} and Nd^{3+} complexes.

$$\text{uniformity score} = \sqrt{(\theta - \theta_{\text{ideal}})^2 + (\Phi - \Phi_{\text{ideal}})^2} \quad (1)$$

The score gives a measure of how far the two sets of values are from each other; the smaller the score the closer to ideality is the complex' geometry. To provide some context, a score of 100° would correspond to bending and twisting of 135 and 45° , respectively, which reasonably represent the maximum chemical distortion achievable. And a score of 0° would correspond to a perfectly linear complex with no twisting (D_{4d} symmetry in this case). As shown in Figure 3, all the Cm^{3+} complexes, except with PW_{11} , have a score of 2.5 to 4° . The relatively low score indicates that the Cm^{3+} complexes with BW_{11} , SiW_{11} , GeW_{11} , and GaW_{11} have near-ideal geometry and are very uniform. In contrast, the Eu^{3+} complexes scored between 16.9° and 23.4° , with only GeW_{11} scoring at 3.2° . It is thus reasonable to conclude that the $\text{Cm}(\text{XW}_{11})_2$ structures are far more uniform than the $\text{Eu}(\text{XW}_{11})_2$ analogous structures with respect to the central f -element. The same conclusions can be drawn for the Am^{3+} versus Nd^{3+} complexes. These two series of apparently similar structures, obtained under identical conditions, therefore demonstrate that trivalent actinides and lanthanides exhibit independent “beyond first sphere” coordination chemistries, with specificities that manifest not necessarily in the first coordination sphere (all structures studied here are 8-coordinated and have the same speciation $\text{M}(\text{XW}_{11})_2$) but throughout the structure of their compounds.

To confirm our analysis of the coordination geometry around Eu^{3+} and Cm^{3+} , continuous symmetry operation measurements were performed, using the computer code recently published by Nielsen et al.³⁵ The results are available in Figure S4 and showcase that Cm^{3+} are closer to the ideal square antiprism geometry than Eu^{3+} . The trend was confirmed with an analysis of the Nd^{3+} and Am^{3+} structures with the five POMs as well. Such effects could not be observed by just focusing on metal–oxygen bond distances or for a single structure, as is often the case in actinide coordination chemistry studies.

Rationalizing the Solid-State and Solution-State Luminescence of Eu-POM Complexes and the Role of Counterions (Li^+ , Na^+ , K^+ , Rb^+ , and Cs^+). In order to rationalize the structural effects observed in the $\text{Ln}(\text{XW}_{11})_2$ and $\text{An}(\text{XW}_{11})_2$ structures (*vide supra*), we also investigated the impact of the alkali counterions by leveraging Eu^{3+} and Cm^{3+} luminescence properties. We previously observed, in a smaller POM complex ($[\text{Cm}(\text{W}_5\text{O}_{18})_2]^{9-}$), that the Cm^{3+} ion luminescence was impacted by the presence of Na^+ versus Cs^+ in solution.³⁰ The five POMs studied here were found to be efficient luminescence sensitizers for both Eu^{3+} and Cm^{3+} via excitation in the POM band at ~ 300 nm (see Figures S6 and S7 for all excitation and emission spectra). We therefore hypothesized that probing the impact of the alkali ions on the $\text{M}(\text{XW}_{11})_2$ complexes would provide an additional magnification tool to identify the differences between heavy actinides and lanthanides. Obtaining a full series of comparable crystal

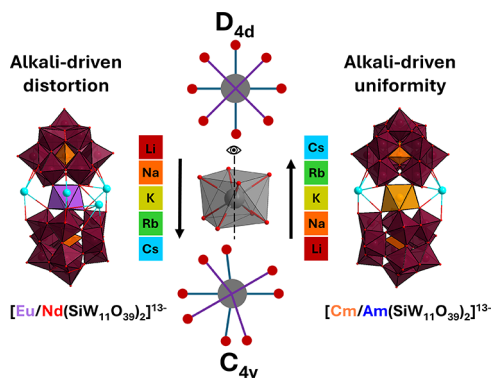


Figure 4. Polyhedral representations of $\text{Eu}(\text{SiW}_{11})_2$ with its four equatorial Cs^+ atoms and $\text{Cm}(\text{SiW}_{11})_2$ with its two equatorial Cs^+ counterions. A ball and stick representation of the site symmetry for Eu^{3+} or Cm^{3+} is also shown, with the different trends observed along the alkali series.

structures for Cm^{3+} and Eu^{3+} , with the five XW_{11} ligands and the five possible alkali ions (Li^+ , Na^+ , K^+ , Rb^+ , and Cs^+), would be ideal. However, given radiological constraints associated with curium isotopes (^{248}Cm plus ^{246}Cm in our case), the inevitable

generation of long-lived radioactive waste, the isotope rarity, and the higher solubility of the $\text{M}(\text{XW}_{11})_2$ complexes with light alkalis, we did not attempt to crystallize the 25 compound combinations (5 alkalis times 5 XW_{11} POMs). Nevertheless, we characterized the obtained single crystals with Cs^+ and the five POMs via solid-state luminescence (emission, excitation, and lifetime measurements) for both Eu^{3+} (Figure 5a) and Cm^{3+} (Figure 7a). Additionally, we took on solution-state characterization of the 25 combinations for both Eu^{3+} (Figure 5b,c) and Cm^{3+} (Figure 7b,c). Characteristic examples of this large luminescence spectroscopy data set are given in Figure 6, with the full data set of emission and excitation spectra given in Figures S6 for Eu^{3+} and Figure S7 for Cm^{3+} . Peak intensity ratios are also given in Tables S9 and S10.

Due to the strong ion pairing between the XW_{11} and the alkali series,^{36,37} we can approximate the solid-state behavior through solution-state luminescence characterization and correlate physiochemical properties. To establish the role that alkali counterions have on the geometry of the complexes (if any), we must first understand the single crystal luminescence of $\text{Eu}(\text{XW}_{11})_2$ and of $\text{Cm}(\text{XW}_{11})_2$. Spectroscopy on single crystals has the advantage of direct knowledge of the site symmetry for Eu^{3+} and Cm^{3+} . As such, we gain information about the crystal

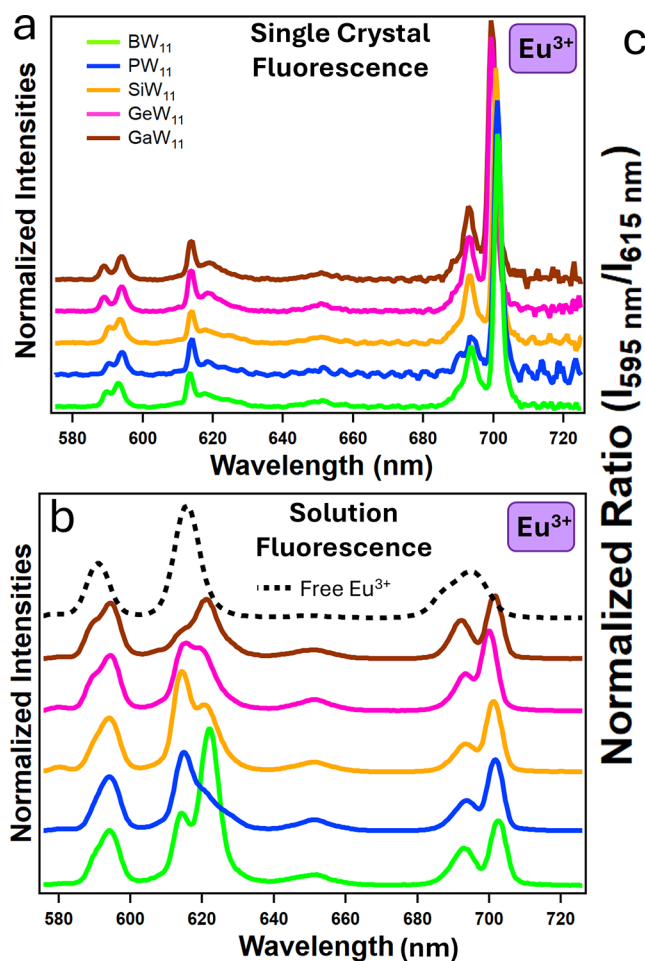


Figure 5. Solid-state and solution-state luminescence spectra of $\text{Eu}(\text{XW}_{11})_2$, with $\text{X} = \text{B}, \text{Si}, \text{P}, \text{Ge}$, or Ga . (a) Single crystals of $\text{Eu}(\text{XW}_{11})_2$. (b) Aqueous solutions of 1 mM $\text{Eu}(\text{XW}_{11})_2$ in 0.1 M acetate buffer at pH 5; $[\text{CsCl}] = 500$ mM. The black curve corresponds to the free Eu^{3+} in solution. (c) Normalized intensity ratio (transitions: $^5\text{D}_0 \rightarrow ^7\text{F}_2$ / $^5\text{D}_0 \rightarrow ^7\text{F}_1$) for the $\text{Eu}(\text{XW}_{11})_2$ complexes in solution and in the presence of the different alkali counterions. See Figure S6 for the full emission and excitation spectra. Note that the small wiggles in panel (b) are due to instrumental interference fringes with glass substrate used for the measurement. See Tables S9 and S10 for tabulated values.

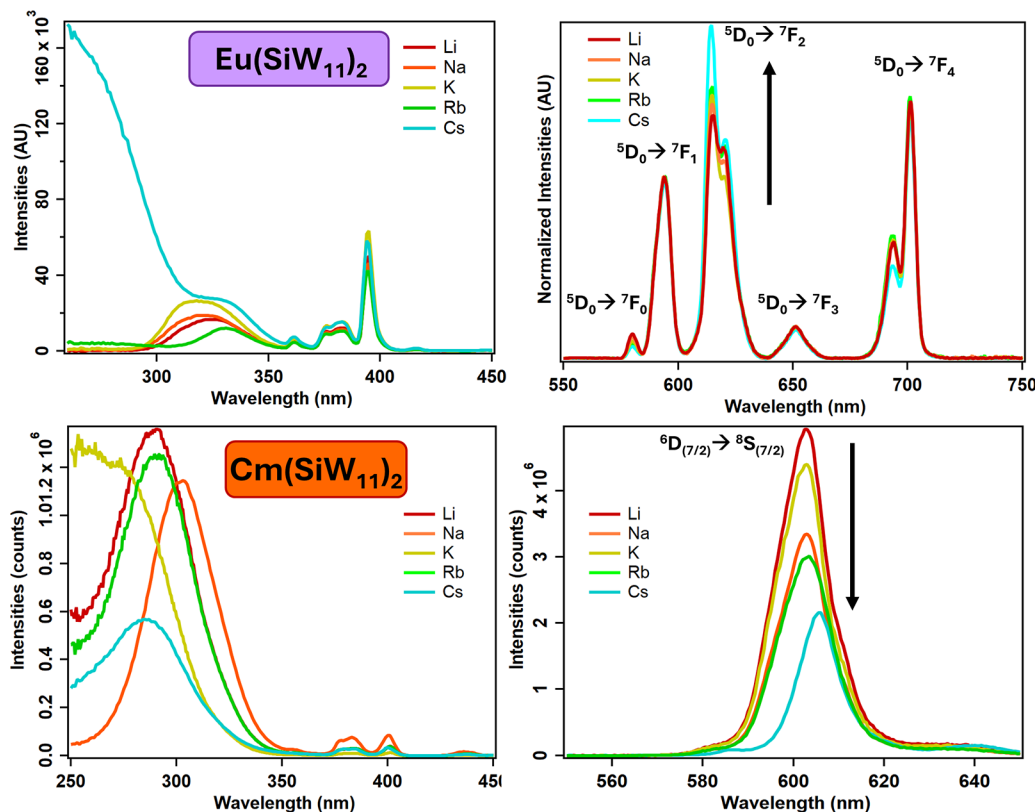


Figure 6. Example of solution luminescence spectra of Eu-POM (top row) and Cm-POM (bottom row) complexes with five different alkali counterions. POM = $\text{SiW}_{11}\text{O}_{39}^{8-}$. See Figure S7 for full emission and excitation spectra. Excitation spectra (left) and emission spectra (right) for the Eu and Cm SiW_{11} as a function of the alkali counterion. Light blue curves: Cs^+ . Green curves: Rb^+ . Kaki curves: K^+ . Orange curves: Na^+ . Red curves: Li^+ . Samples were aqueous solutions at pH 5.5 (0.1 M acetate buffer). $[\text{Eu}] = 1 \text{ mM}$. $[\text{Cm}] = 100 \mu\text{M}$. $[\text{POM}] = 200 \mu\text{M}$ for Cm and 2 mM for Eu. $[\text{Alkali}] = 250 \text{ mM}$ for Eu and 2.5 mM for Cm. See Tables S9 and S10 for tabulated values.

field that imposes the D_{4d} geometry on Eu^{3+} or Cm^{3+} within the $\text{M}(\text{XW}_{11})_2$ structures. By extension, we can also gain knowledge on any distortions to the geometry thereof. The $\text{Eu}(\text{XW}_{11})_2$ structures become an excellent benchmark as Eu^{3+} luminescence has been extensively studied in both solution and solid states.^{38–41} Therefore, based on the expected D_{4d} symmetry for Eu^{3+} , we should expect the following:

1. $^5\text{D}_0 \rightarrow ^7\text{F}_0$ forbidden transition should appear as a weak or absent peak;
2. $^5\text{D}_0 \rightarrow ^7\text{F}_1$ magnetic dipole allowed transitions should appear as two peaks;
3. $^5\text{D}_0 \rightarrow ^7\text{F}_2$ hypersensitive transition, which is forbidden under D_{4d} symmetry, but appears as two peaks under C_{4v} symmetry;
4. $^5\text{D}_0 \rightarrow ^7\text{F}_3$ forbidden transition should appear as a weak or absent peak;
5. $^5\text{D}_0 \rightarrow ^7\text{F}_4$ induced magnetic dipole transitions.

Figure 5a shows the emission spectra of single crystals of $\text{Cs}-\text{Eu}(\text{XW}_{11})_2$ (for which the structures were determined, *vide supra*), and Figure 5b shows the corresponding spectra of the $\text{Eu}(\text{XW}_{11})_2$ complexes in aqueous solutions containing excess Cs^+ ions. In the single crystal spectra, the most discernible features are the intense peaks around 680–710 nm ($^5\text{D}_0 \rightarrow ^7\text{F}_4$ transition), followed by the less intense peaks at around 610–630 nm ($^5\text{D}_0 \rightarrow ^7\text{F}_2$) and 585–600 nm and ($^5\text{D}_0 \rightarrow ^7\text{F}_1$). Small peak shifts are observed among the POMs, with the peak maxima of the $^5\text{D}_0 \rightarrow ^7\text{F}_4$ transition being as follows: $\text{Eu}(\text{BW}_{11})_2$ 700.7 nm; $\text{Eu}(\text{PW}_{11})_2$ 701.2 nm; $\text{Eu}(\text{SiW}_{11})_2$ 701.7 nm;

$\text{Eu}(\text{GeW}_{11})_2$ 699.3 nm; $\text{Eu}(\text{GaW}_{11})_2$ 699.3 nm. All the reported spectra here are consistent with previously reported spectra for PW_{11} and GeW_{11} ,^{42,43} and it is consistent with geometry seen around Eu^{3+} in the crystal structures. It is worth noting again that under D_{4d} symmetry, the $^5\text{D}_0 \rightarrow ^7\text{F}_2$ transition is forbidden by theory. However, this is much like the forbidden $^5\text{D}_0 \rightarrow ^7\text{F}_0$ and $^5\text{D}_0 \rightarrow ^7\text{F}_3$ transitions, which are still observed due to minor geometric distortions, J -mixing, and thermal motion (results were collected at room temperature). In the solution spectra (Figure 5b), the $^5\text{D}_0 \rightarrow ^7\text{F}_0$ and $^5\text{D}_0 \rightarrow ^7\text{F}_3$ transitions are observed, though weakly due to the “weaker” crystal field imposed when the complexes are in solution and in dynamic exchange. Only the $^5\text{D}_0 \rightarrow ^7\text{F}_2$ transition is present in the single crystals and solution-state spectra. Nevertheless, the presence of the $^5\text{D}_0 \rightarrow ^7\text{F}_2$ and the very intense $^5\text{D}_0 \rightarrow ^7\text{F}_4$ peak in the single crystal luminescence spectra strongly suggest that there is a lack of an inversion center, which implies a distortion of the D_{4d} site symmetry. Since the luminescence spectra were obtained from the same crystals the structural data was collected on, we can conclude that the site symmetry for Eu^{3+} is a distorted D_{4d} or, more accurately, a C_{4v} (Figure 4).

When the single crystal spectra are then compared with the solution spectra, similar features are observed (Figure 5a-b). The main difference, however, is a less intense $^5\text{D}_0 \rightarrow ^7\text{F}_4$ transition (680–710 nm), comparable in intensity to the $^5\text{D}_0 \rightarrow ^7\text{F}_2$ transition. This suggests that in solution, the Eu^{3+} ion is still under a relatively strong crystal field imposed by the POM ligands but not as strong as the one imposed by the entirety of the crystal structure. A good indicator of the strength of the

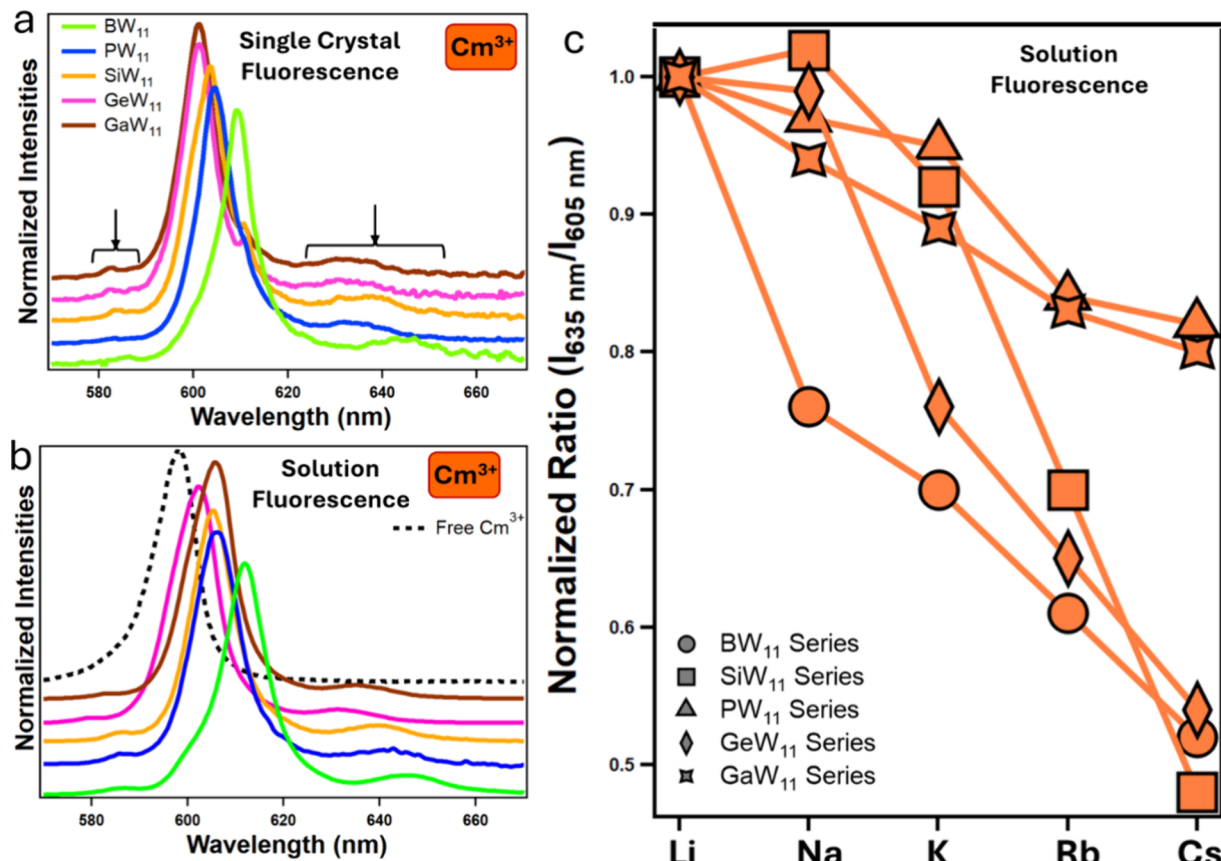


Figure 7. Solid-state and solution-state luminescence emission spectra of $\text{Cm}(\text{XW}_{11})_2$ complexes, with $\text{X} = \text{B}, \text{Si}, \text{P}, \text{Ge}$, or Ga . (a) Single crystals of $\text{Cs}-\text{Cm}(\text{XW}_{11})_2$. Arrows indicate the range of usually not observed transitions. (b) Solution-state emission; $50 \mu\text{M} \text{Cm}(\text{XW}_{11})_2$ in 0.1 M acetate buffer at pH 5.5. $[\text{CsCl}] = 2.5 \text{ mM}$. (c) Normalized intensity ratio (transitions: $635 \text{ nm}/605 \text{ nm}$) for the $\text{Cm}(\text{XW}_{11})_2$ complexes in solution and in the presence of the five different alkali counterions. $[\text{Alkali}] = 2.5 \text{ mM}$. See Figure S7 for full emission and excitation spectra. See Tables S7–S10 for tabulated values.

crystal field is the splitting of the $^5\text{D}_0 \rightarrow ^7\text{F}_1$, as previously used for Eu^{3+} complexes with organic ligands.⁴⁴ Deconvolution and peaking fitting of this transition in the Eu-POMs show the presence of two peaks, which is shown in Table S11. Previous work by Sorensen et al.^{40,44,45} described the splitting of the $^5\text{D}_0 \rightarrow ^7\text{F}_1$ transition in Eu^{3+} complexes as three peaks for three split states, but the authors pointed out some states might be degenerate and overlap, which is what is observed here, with two peaks resolved at 590 and 594 nm, approximately. Taking the ratio of the peak height shows that the intensity of the split changes from solution to solid state and across the series of heteroatoms, with BW_{11} providing the most intense split, both in solution and solid-state (Table S11). Interestingly, even though the $^5\text{D}_0 \rightarrow ^7\text{F}_2$ transition is technically still forbidden under D_{4d} symmetry, it is observed in the solution spectra, which is another indicator of distortion of the site symmetry for Eu^{3+} but not an indicator of the crystal field strength.

When the rest of the $\text{Eu}(\text{XW}_{11})_2$ complexes were studied in the presence of different alkali counterions (Figure 5c, Figure S6, Tables S9 and S10), a trend where the intensities of the $^5\text{D}_0 \rightarrow ^7\text{F}_2$ transition changes as a function of the alkali counterion (Li^+ to Cs^+) became obvious. The intensity trend was further quantified by normalizing all spectra to the $^5\text{D}_0 \rightarrow ^7\text{F}_1$ transition across the five POMs, followed by calculating the intensity ratio of the transitions $^5\text{D}_0 \rightarrow ^7\text{F}_2 / ^5\text{D}_0 \rightarrow ^7\text{F}_1$ (Figure 5c). An increasing ratio means the $^5\text{D}_0 \rightarrow ^7\text{F}_2$ transition is becoming predominant – implying a deviation from the D_{4d} site symmetry. The plotted ratios (Figure 5c) clearly show that, for the five

series of $\text{Eu}(\text{XW}_{11})_2$ complexes, moving from Li^+ to Cs^+ increases the intensity ratio $^5\text{D}_0 \rightarrow ^7\text{F}_2 / ^5\text{D}_0 \rightarrow ^7\text{F}_1$, suggesting some distortion occurs around Eu^{3+} as the alkali counterion gets heavier. $\text{Eu}(\text{GeW}_{11})_2$ appears to be somewhat an exception as it is less impacted by the nature of the alkali, but this is likely because the complex is already very close to an ideal D_{4d} symmetry (Lowest score within the Eu structures, see Figure 3a). The conclusion thus becomes that moving from Li^+ to Cs^+ distorts the symmetry around Eu^{3+} , from D_{4d} to C_{4v} , with GeW_{11} being the least impacted. This is congruent with the single crystal structures and calculated parameters for $\text{Eu}(\text{XW}_{11})_2$ (Figure 2).

Since the polytungstate ligands allow for efficient coordination and luminescence for Eu^{3+} and Cm^{3+} , the alkali counterions are not typically considered to be interacting or to provide relaxation pathways impacting emission properties. However, from the luminescence and crystallography results presented herein, it is thus reasonable to conclude that the alkali counterions do interact with the complexes, and while having seemingly subtle impacts on the geometry, they have a measurable influence on the f-element luminescence properties.

Advancing Curium Chemistry and Deciphering Its Luminescence Properties. Having defined the effects the alkali counterions have on the geometry and physicochemical properties of the $\text{Eu}(\text{XW}_{11})_2$ complexes, we attempted to discern these effects in $\text{Cm}(\text{XW}_{11})_2$. Figure 7a shows the emission spectra for single crystals of the $\text{Cs}-\text{Cm}(\text{XW}_{11})_2$ complexes, and Figure 7b shows solution-state spectra of the

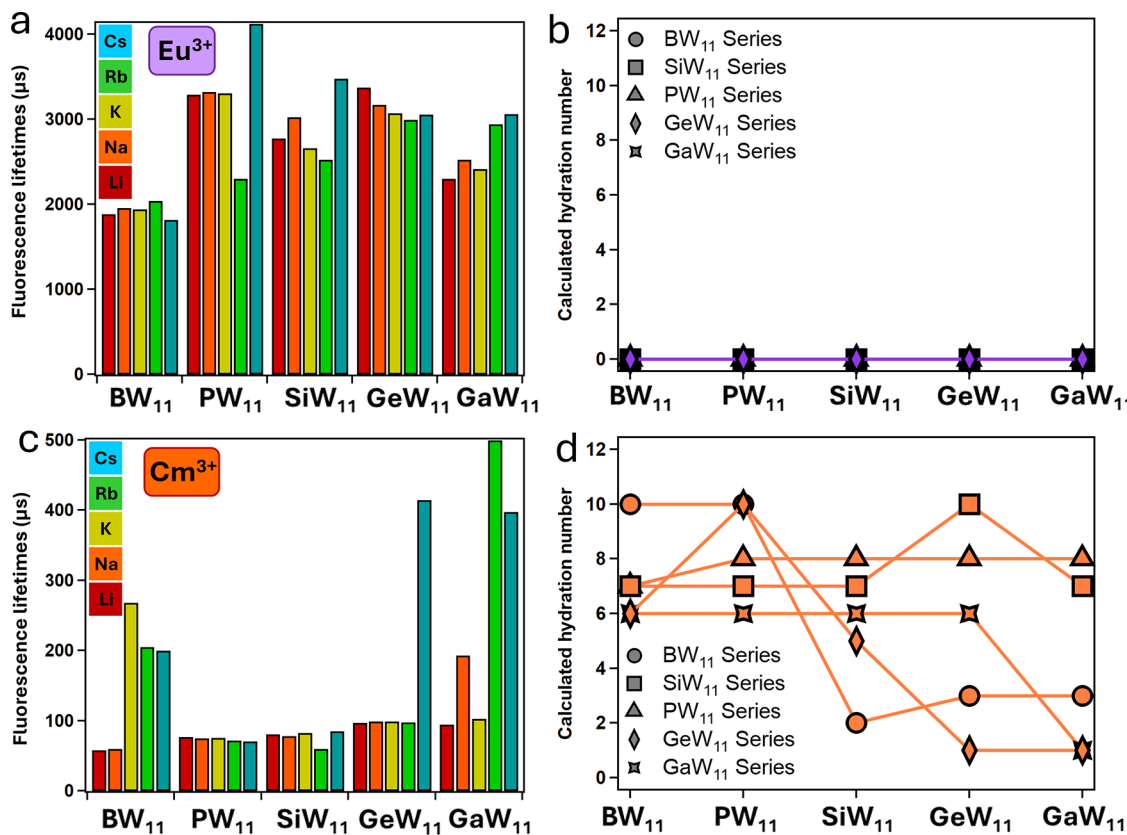


Figure 8. Solution state luminescence lifetimes of the alkali-Eu-POM and alkali-Cm-POM systems. Alkali = Li⁺, Na⁺, K⁺, Rb⁺, or Cs⁺. (A) Luminescence lifetime of the [Eu(XW₁₁)]ⁿ⁻complexes. (B) Calculated number of water molecules coordinated to Eu, using the Kimura equation. C) Luminescence lifetime of the [Cm(XW₁₁)]ⁿ⁻complexes. Note that the Y-axes in panels (a) and (b) are not the same, as the Cm³⁺lifetimes are typically shorter than the Eu³⁺ones. (D) Calculated number of water molecules coordinated to Cm, using the Kimura equation.⁵⁴ Tabulated values are in Tables S12 and S13.

curium complexes in the presence of excess Cs⁺ counterions. Contrasting with the behavior of the Eu(XW₁₁)₂ complexes, the spectra for the five Cm(XW₁₁)₂ complexes are almost identical in the solid state and solution state. Relative to Eu³⁺, larger shifts for the main Cm³⁺ emission peak were also observed across the POM series: Cm(BW₁₁)₂ 609.3 nm; Cm(PW₁₁)₂ 604.3 nm; Cm(SiW₁₁)₂ 603.3 nm; Cm(GeW₁₁)₂ 601.7 nm; Cm(GaW₁₁)₂ 601.7 nm.

Otherwise, subtle differences were observed in the solid state, such as slightly thinner and more pronounced shoulder peaks. The three main Cm³⁺ emission peaks were observed in both the single crystal and solution spectra: 585, 601–609, and 635 nm (Figure 7a,b). Interestingly, while several studies^{12,22,24,46–51} have been published on Cm³⁺ luminescence in solution, it should be noted that most complexes are not 8-coordinated nor highly symmetrical like the Cm(XW₁₁)₂ complexes. The vast majority (if not all) of the aqueous Cm³⁺ complexes previously studied are 9-coordinated and present in a distorted environment. Most previously studied complexes also contain water molecules coordinated to Cm³⁺, resulting in significant quenching of the luminescence emission signal. Finally, most reported Cm³⁺ emission spectra were collected only between ~580 and ~630 nm. This is mostly likely due to the 601–609 nm peak, which is the primary emissive peak, corresponding to the $^6D_{7/2} \rightarrow ^8S_{7/2}$ transition. However, upon a strong crystal field imposed by the POM ligands, the ground state, along with other states, can split.

A key observation that will be discussed below is the relationship between potential vibronic-coupled emission peaks and the symmetry around Cm³⁺. The underlying hypothesis is that the new split states are within the range of key vibrational states. This overlap between electronic and vibrational states could allow for the observation of new luminescence pathways. These new pathways take form in minor but distinct emissions peaks for Cm³⁺ at ~585 and ~635 nm (arrows, Figure 7a). In solution, the emission at ~585 and ~635 nm is not present in the spectrum of the free Cm³⁺ ion measured under similar conditions (Figure 7b), and its emission peak appears as the usual broad transition, different from what is observed with the Cm-POM complexes. However, the emission spectra from the Cm-POMs (solid-state and in solution) are consistent with the solid-state luminescence emission spectra of Cm³⁺-doped ThO₂ at room temperature and liquid helium temperature, as previously reported in the pioneering work of Thouvenot, Hubert, and Edelstein⁵² and, then by Liu et al.⁵³ with Cm³⁺-doped LuPO₄, where, upon cooling the Cm-doped solids, the peaks at 585 and 635 nm disappeared, confirming the phonon-assisted nature of these transitions. It is worth mentioning that phonon-assisted transitions and vibronic transitions are similar to each other, as they couple vibrational states with the electronic transitions. However, vibronic transition is the coupling of molecular vibrations, within the [Cm(XW₁₁)₂]ⁿ⁻, and electronic transitions (hence possible in diluted matrices and solids), whereas the phonon-assisted transition is the coupling of lattice vibrations to electronic transitions.

Within the context of $\text{Cm}(\text{XW}_{11})_2$ complexes reported here, we analyzed the 25 combinations of $\text{Cm}(\text{XW}_{11})_2$: five POMs ($\text{X} = \text{B}, \text{Si}, \text{P}, \text{Ge}, \text{Ga}$) with five alkali counterions in solution (Figure 7c and Figure S7). If the peaks at 585 and 635 nm arise from the coupling of vibrational states and electronic transitions, then (1) undergoing the same alkali counterion exchange as Eu^{3+} (Figure 4) should reveal the same symmetry distortion going down the alkali group; and (2) the ratio of the intensities for the peaks at 601–609 and 635 nm would change as well. Unexpectedly, while there are noticeable changes in the intensities between both peaks (Figure 5), the trend for Cm^{3+} is opposite to what is observed for Eu^{3+} (Figure 5c vs Figure 7c). The intensity trend was quantified by normalizing all spectra to the main peak at 601–609 nm, followed by calculating the ratio of the intensities for the peaks at 601–609 nm divided by that of the peak at 635 nm (Figure 7c). The ratios herein decreased, meaning that the peak at 635 nm becomes more prominent when moving from Li^+ to Cs^+ . In contrast to Eu^{3+} , this corresponds to an improvement of the symmetry around Cm^{3+} , converging toward an ideal D_{4d} and potentially increasing the coupling between vibrational states and electronic transitions. Hence, the impact of the alkalis on $\text{Cm}(\text{XW}_{11})_2$ compounds is opposite to what is observed for their Eu^{3+} counterparts, with an improvement of the symmetry around Cm^{3+} as the alkali counterion gets heavier. This is congruent with the crystal structures obtained with Cs^+ counterions which are more uniform in the case of Cm^{3+} compared to Eu^{3+} (Figure 3a).

Time-Resolved Luminescence Properties of the 50 Complexes Alkali-Eu(XW_{11}) and Alkali-Cm(XW_{11}), with $\text{Li}^+, \text{Na}^+, \text{K}^+, \text{Na}^+, \text{Rb}^+, \text{Cs}^+$ and $\text{X} = \text{B}^{3+}, \text{Si}^{4+}, \text{P}^{5+}, \text{Ge}^{4+}, \text{Ga}^{3+}$. Time-resolved luminescence emission experiments were also performed. For the solutions, the luminescence lifetime, herein denoted by τ , was measured for the 25 combinations (five POMs times five alkalis) for both Eu^{3+} and Cm^{3+} . The results are summarized in Figure 8, and the tabulated values are given in Tables S12–S14. In solution, the predominant species, i.e., $[\text{Eu}(\text{XW}_{11})_2]^{n-}$, had a τ of 1817 to 4123 μs , while the minor component (0% for BW_{11} and GaW_{11} , < 12% for PW_{11} , < 23% for SiW_{11} , and < 32% for GeW_{11}), corresponding to the 1:1 complex $[\text{Eu}(\text{XW}_{11})]^{n-}$, had a τ of 253 to 857 μs (Table S12).

Considering the Kimura equation,⁵⁴ which empirically correlates the number of complexing water molecules to Eu^{3+} with the observed luminescence emission lifetime, the calculated number of H_2O is zero for the dominant species, $[\text{Eu}(\text{XW}_{11})_2]^{n-}$, for the five POMs and the five alkali options (Figure 8b). This is consistent with the Eu-POM crystal structures (and also Nd-POMs, *vide supra*). The shortest lifetime measured was for $\text{Cs}-\text{Eu}(\text{BW}_{11})_2$ in solution, at 1817 μs , while the other $\text{Cs}-\text{Eu}(\text{XW}_{11})_2$ complexes had values greater than 3000 μs . Interestingly, the lifetime trends tend to follow the structural parameter related to the stretching of the complex (δ – Figure 2a), with longer δ and lower symmetry resulting in shorter lifetimes. For the minor species, i.e., $[\text{Eu}(\text{XW}_{11})]^{n-}$, the lifetimes and Kimura equation yield between 1 and 4 water molecules, depending on the POM and alkali (Table S12). One would expect the $[\text{Eu}(\text{XW}_{11})]^{n-}$ complex to have a hydration number of 4 because the XW_{11} POMs are tetradentate ligands, and the Eu^{3+} usually needs eight neighbors to complete its coordination sphere. Here, we note that the calculated number of molecules for the $[\text{Eu}(\text{XW}_{11})]^{n-}$ complex tends to be smaller when the counterion used in the solution goes from Li^+ to Cs^+ (Table S12). For example for $[\text{Eu}(\text{SiW}_{11})]^{5-}$, the calculated hydration number goes from 4 with $\text{Li}^+, \text{Na}^+, \text{K}^+$ to only 2 with

Rb^+ , and Cs^+ . The most plausible explanation is that the Cs^+ or Rb^+ counterion's strong ion pairing with the POM ligands can alter luminescence pathways of the f-element complexed to the POM, resulting in different lifetimes. While the Kimura equations⁵⁴ have been widely used in the f-element community, they have not been developed by taking into account potential effects in tertiary systems like counterion/ligand/f-element, with second-order interactions between counterions and ligands. Furthermore, none of the original data sets upon which these empirical equations were built contained POM ligands. It is therefore likely that the alkali/POM/f-element systems studied here are at the frontier of validity of this empirical model.

The departure from nonideal behavior becomes more apparent with curium. Unlike Eu^{3+} , the Kimura equation fails to correlate the number of complexing waters to the measured lifetime for Cm^{3+} . As shown in Figure 8d, when considering the longest lifetime measured for curium (i.e., $[\text{Cm}(\text{XW}_{11})_2]^{n-}$ species), the calculated hydration number ranges from 1 to 10. This is at odds with the expected speciation and obtained crystal structures and indicates that the Kimura equation is no longer valid to describe the alkali-Cm-POM systems. As such, arriving at some generalizations for the Cm^{3+} emission lifetime trends becomes somewhat more complex. Lifetimes were also measured for each peak, 585, 601–609, and 635 nm, across the five Cs-Cm-POM single crystals (Table S13). The main transition, at 601–609 nm, had the longest lifetimes $\tau = 263$ –377 μs . The peaks at 585 and 635 nm instead had two fitted lifetimes: $\tau_1 = 102$ –342 μs and $\tau_2 = 15$ –150 μs . These two different lifetimes measured at 585 and 635 nm are consistent with the values seen in solution (Table S13). Usually, the presumption upon seeing different lifetime values is the presence of different species, like 1:1 and 1:2 complexes discussed, *vide supra*. However, in the context of Cm^{3+} , we observed different values for different peaks on a system that, through single crystal diffraction, reveals only one Cm^{3+} species, the $[\text{Cm}(\text{XW}_{11})_2]^{n-}$. Therefore, the only reasonable conclusion upon seeing different lifetimes for Cm^{3+} arises from different luminescence pathways within the complexes. This supports the hypothesis that the transitions at 585 and 635 nm observed in Cm-POM complexes could be a combination of vibronic-coupled emission peaks and new emissive pathways made observable because of the high symmetry of these complexes.

CONCLUSIONS

The results presented here showcase that it is possible to isolate and characterize series of isostructural complexes for lanthanide and heavy actinide complexes, as confirmed through single crystal X-ray structures of Nd-POM, Eu-POM, Am-POM, and Cm-POM complexes. This study provides a series of heavy actinide complexes structurally characterized and with elements rarely seen in actinide chemistry ($\text{B}^{3+}, \text{Ga}^{3+}, \text{Si}^{4+}, \text{Ge}^{4+}$, or P^{5+}). While the general compound formulas can be similar for Eu^{3+} versus Cm^{3+} (and Nd^{3+} versus Am^{3+}), their solid-state and solution-state coordination chemistries as well as physiochemical properties can deviate significantly. The solution-state characterization, via steady-state and time-resolved luminescence of the Cm-POM and Eu-POM complexes with the five different POM ligands and with five different counterions ($\text{Li}^+, \text{Na}^+, \text{K}^+, \text{Rb}^+$, or Cs^+) offered one of the most complete spectroscopic data sets comparing a heavy actinide and a lanthanide. The serial approach taken here allowed magnifying differences between actinides and lanthanides, notably in regard to the complexes' uniformity, symmetry deformation in

response to counterions, and luminescence lifetime trends. The diverging structural and spectroscopic properties between Eu³⁺ versus Cm³⁺ and Nd³⁺ versus Am³⁺ demonstrate that lanthanides are only an approximation for transuranic elements. While lanthanide may provide useful information, actinides have been shown to be different enough, so as to warrant their own investigations.

■ EXPERIMENTAL SECTION

Caution! ^{248/247/246}Cm, as well as their decay products, constitute serious health hazards because of their radioactive and chemical properties. All experiments involving radionuclides were conducted at Lawrence Livermore National Laboratory, in facilities designed for the safe handling of long-lived and short-lived radioactive materials and associated waste.

Materials. Curium samples (97% ²⁴⁸Cm + 3% ²⁴⁶Cm + 0.01% ²⁴⁷Cm) were prepared from a primary source purchased from Oak Ridge National Laboratory (USA) and ²⁴³Am(III) chloride purchased from Eckert & Ziegler (USA). Europium chloride (\geq 99.9%), NaCH₃COO (\geq 99.9%), cesium chloride (>99.99%), Na₂WO₄·2H₂O (\geq 99%), phosphoric acid, sodium metasilicate (\geq 99%), germanium oxide (\geq 99%), gallium nitrate (\geq 99%) were purchased from chemical providers (VWR and Millipore Sigma) and used as received. All solutions were prepared using deionized water purified by reverse osmosis cartridge system (\geq 18.2 MΩ·cm). All experiments were performed in a temperature-controlled room (22 °C).

Synthesis. Lanthanide or actinide chloride salts (^{246/248}Cm³⁺/²⁴³Am³⁺ from a parent stock solution in HCl) are added to a 200 μM XW₁₁ (40 μM for Am³⁺) solution in 0.1 M acetate buffer at pH 5.5. A 1:2 stoichiometric addition of lanthanide or actinide was made to PW₁₁ (concentrations for lanthanides and actinides were kept in the 50–100 μM range). For crystallization, 6 M CsCl is titrated in (5–50 μL) to 1:2 stoichiometric solutions (10 to 100 μL, at pH 5.5, 100 mM acetate buffer). After 1–5 days of ambient conditions, several single crystals were visible to the naked eye. Upon inspection with an optical microscope, XRD-quality crystals are mounted and characterized via small molecule single crystal XRD, while the rest are kept for further analysis via luminescence spectroscopy.

Crystallography. All structures were collected using a Rigaku Synergy Custom single crystal diffractometer, equipped with a kappa goniometer and using Mo Kα radiation ($\lambda = 0.71073 \text{ \AA}$) with a fwhm of $\sim 200 \mu\text{m}$ at the sample from a MicroMax-007 HF microfocus rotating anode source. Images were recorded on a Dectris Pilatus 3R (300 000 – CdTe) detector and processed using CrysAlisPro. After integration, both analytical absorption and empirical absorption (spherical harmonic, image scaling, and detector scaling) corrections were applied.⁵⁵ All structures were solved by the intrinsic phasing method from SHELXT program,⁵⁶ developed by successive difference Fourier syntheses, and refined by full-matrix least-squares on all F² data using SHELX42 via OLEX2 interface.⁵⁷ Crystallographic information for the six reported structures can be obtained free of charge from the Cambridge Crystallographic Data Center (<https://www.ccdc.cam.ac.uk/>) upon referencing CCDC numbers in the crystallographic tables below.

Luminescence Spectroscopy. Steady-state and time-resolved spectra were measured with an FLS1000 spectrometer (Edinburgh Instruments) equipped with a double monochromator on the excitation and emission arms. A 450 W xenon lamp was used as a light source for the steady-state measurements, and a 60 W microsecond flashlamp was used for lifetime measurements (multichannel scaling single photon counting mode). Each lifetime decay curve contained 2000 data points, with the maximum count per channel set to at least 1000. The timespan of the acquisition was set so that the signal was measured until its return to the background level. Luminescence data for liquid samples were measured in sealed quartz cuvettes, and the emission was collected at 90° relative to the excitation. Lifetimes were fitted by using the Fluororacle computer program (Edinburgh Instruments). Solid State fluorescence was undertaken using a CRAIC Microspectrophotometer using an LED excitation centered at 365 nm.

■ ASSOCIATED CONTENT

SI Supporting Information

The Supporting Information is available free of charge at <https://pubs.acs.org/doi/10.1021/jacs.Sc00861>.

Abbreviation list, summary of structures obtained, chemical formula, and associated CCDC numbers, additional experimental section, detailed crystallography data collection data and analysis, additional structure visualizations, fluorescence data sets for alkali-Eu-POM systems and alkali-Cm-POM systems, and supplementary references ([PDF](#))

Accession Codes

Deposition Numbers 2376391–2376396, 2423540–2423543, and 2428567–2428568 contain the supplementary crystallographic data for this paper. These data can be obtained free of charge via the joint Cambridge Crystallographic Data Centre (CCDC) and Fachinformationszentrum Karlsruhe Access Structures service.

■ AUTHOR INFORMATION

Corresponding Authors

Ian Colliard – Physical and Life Sciences Directorate, Glenn T. Seaborg Institute and Material Sciences Division, Lawrence Livermore National Laboratory, Livermore, California 94550, United States; Email: Colliard1@LLNL.gov

Gauthier J.-P. Deblonde – Nuclear and Chemical Sciences Division and Physical and Life Sciences Directorate, Glenn T. Seaborg Institute, Lawrence Livermore National Laboratory, Livermore, California 94550, United States;  orcid.org/0000-0002-0825-8714; Email: Deblonde1@LLNL.gov

Complete contact information is available at:

<https://pubs.acs.org/10.1021/jacs.Sc00861>

Notes

The authors declare no competing financial interest.

■ ACKNOWLEDGMENTS

This material is based upon work supported by the U.S. Department of Energy, Office of Science, Office of Basic Energy Sciences, Heavy Element Chemistry program. This manuscript has been authored by Lawrence Livermore National Security, LLC under contract no. DE-AC52-07NA27344 with the U.S. Department of Energy. The United States Government retains, and the publisher, by accepting the article for publication, acknowledges that the United States Government retains a nonexclusive, paid-up, irrevocable, worldwide license to publish or reproduce the published form of this manuscript, or allow others to do so, for United States Government purposes. The authors are grateful to LLNL's Glenn T. Seaborg Institute for access to various instrumentations. The authors also thank Anna M. Johnson (LLNL) for the efficient logistical support of this project. Release number: LLNL-JRNL-2001945.

■ REFERENCES

- (1) Schwerdtfeger, P.; Smits, O. R.; Pykkö, P. The Periodic Table and the Physics That Drives It. *Nat. Rev. Chem.* **2020**, 4 (7), 359–380.
- (2) Cwiok, S.; Heenen, P.-H.; Nazarewicz, W. Shape Coexistence and Triaxiality in the Superheavy Nuclei. *Nature* **2005**, 433 (7027), 705–709.
- (3) Block, M.; Ackermann, D.; Blaum, K.; Droese, C.; Dworschak, M.; Eliseev, S.; Fleckenstein, T.; Haettner, E.; Herfurth, F.; Heßberger, F. P.; Hofmann, S.; Ketelaer, J.; Ketter, J.; Kluge, H.-J.; Marx, G.;

- Mazzocco, M.; Novikov, Y. N.; Plaß, W. R.; Popeko, A.; Rahaman, S.; Rodríguez, D.; Scheidenberger, C.; Schweikhart, L.; Thirolf, P. G.; Vorobyev, G. K.; Weber, C. Direct Mass Measurements above Uranium Bridge the Gap to the Island of Stability. *Nature* **2010**, *463* (7282), 785–788.
- (4) Clery, D. Hopes Evaporate for the Superheavy Element Flerovium Having a Long Life. *Science* **2021**.
- (5) McMillan, E.; Abelson, P. H. Radioactive Element 93. *Phys. Rev.* **1940**, *57* (12), 1185–1186.
- (6) Seaborg, G. T.; McMillan, E. M.; Kennedy, J. W.; Wahl, A. C. Radioactive Element 94 from Deuterons on Uranium. *Phys. Rev.* **1946**, *69* (7–8), 366–367.
- (7) Seaborg, G. T. The Transuranium Elements. *Science* **1946**, *104* (2704), 379–386.
- (8) Seaborg, G. T.; James, R. A.; Ghiorso, A. New Element Curium (Atomic Number 96); AECD-2182; Originating Research Org. not identified, 1948. <https://www.osti.gov/biblio/4421946-new-element-curium-atomic-number> (accessed 2022-01-09).
- (9) Sykora, R. E.; Assefa, Z.; Haire, R. G.; Albrecht-Schmitt, T. E. First Structural Determination of a Trivalent Californium Compound with Oxygen Coordination. *Inorg. Chem.* **2006**, *45* (2), 475–477.
- (10) Cary, S. K.; Vasiliu, M.; Baumbach, R. E.; Stritzinger, J. T.; Green, T. D.; Diefenbach, K.; Cross, J. N.; Knappenberger, K. L.; Liu, G.; Silver, M. A.; DePrince, A. E.; Polinski, M. J.; Van Cleve, S. M.; House, J. H.; Kikugawa, N.; Gallagher, A.; Arico, A. A.; Dixon, D. A.; Albrecht-Schmitt, T. E. Emergence of Californium as the Second Transitional Element in the Actinide Series. *Nat. Commun.* **2015**, *6* (1), 1–8.
- (11) Galley, S. S.; Pattenau, S. A.; Gaggioli, C. A.; Qiao, Y.; Sperling, J. M.; Zeller, M.; Pakhira, S.; Mendoza-Cortes, J. L.; Schelter, E. J.; Albrecht-Schmitt, T. E.; Gagliardi, L.; Bart, S. C. Synthesis and Characterization of Tris-Chelate Complexes for Understanding f-Orbital Bonding in Later Actinides. *J. Am. Chem. Soc.* **2019**, *141* (6), 2356–2366.
- (12) Cary, S. K.; Su, J.; Galley, S. S.; Albrecht-Schmitt, T. E.; Batista, E. R.; Ferrier, M. G.; Kozimor, S. A.; Mocko, V.; Scott, B. L.; Van Alstine, C. E.; White, F. D.; Yang, P. A Series of Dithiocarbamates for Americium, Curium, and Californium. *Dalton Trans.* **2018**, *47* (41), 14452–14461.
- (13) Sperling, J. M.; Warzecha, E.; Windorff, C. J.; Klamm, B. E.; Gaiser, A. N.; Whitefoot, M. A.; White, F. D.; Poe, T. N.; Albrecht-Schönzart, T. E. Pressure-Induced Spectroscopic Changes in a Californium 1D Material Are Twice as Large as Found in the Holmium Analog. *Inorg. Chem.* **2020**, *59* (15), 10794–10801.
- (14) Sperling, J. M.; Beck, N.; Scheibe, B.; Bai, Z.; Brannon, J.; Gomez-Martinez, D.; Grödler, D.; Johnson, J. A.; Lin, X.; Rotermund, B. M.; Albrecht-Schönzart, T. E. Synthesis, Characterization, and High-Pressure Studies of a 3D Berkelium(III) Carboxylate Framework Material. *Chem. Commun.* **2022**, *58* (13), 2200–2203.
- (15) Gaiser, A. N.; Celis-Barros, C.; White, F. D.; Beltran-Leiva, M. J.; Sperling, J. M.; Salpage, S. R.; Poe, T. N.; Gomez Martinez, D.; Jian, T.; Wolford, N. J.; Jones, N. J.; Ritz, A. J.; Lazenby, R. A.; Gibson, J. K.; Baumbach, R. E.; Páez-Hernández, D.; Neidig, M. L.; Albrecht-Schönzart, T. E. Creation of an Unexpected Plane of Enhanced Covalency in Cerium(III) and Berkelium(III) Terpyridyl Complexes. *Nat. Commun.* **2021**, *12* (1), 7230.
- (16) Goodwin, C. A. P.; Su, J.; Stevens, L. M.; White, F. D.; Anderson, N. H.; Auxier, J. D.; Albrecht-Schönzart, T. E.; Batista, E. R.; Briscoe, S. F.; Cross, J. N.; Evans, W. J.; Gaiser, A. N.; Gaunt, A. J.; James, M. R.; Janicke, M. T.; Jenkins, T. F.; Jones, Z. R.; Kozimor, S. A.; Scott, B. L.; Sperling, J. M.; Wedal, J. C.; Windorff, C. J.; Yang, P.; Ziller, J. W. Isolation and Characterization of a Californium Metallocene. *Nature* **2021**, *599* (7885), 421–424.
- (17) Brenner, N.; Sperling, J. M.; Poe, T. N.; Celis-Barros, C.; Brittain, K.; Villa, E. M.; Albrecht-Schmitt, T. E.; Polinski, M. J. Trivalent F-Element Squarates, Square-Oxalates, and Cationic Materials, and the Determination of the Nine-Coordinate Ionic Radius of Cf(III). *Inorg. Chem.* **2020**, *59* (13), 9384–9395.
- (18) Poe, T. N.; Ramanantoanina, H.; Sperling, J. M.; Wineinger, H. B.; Rotermund, B. M.; Brannon, J.; Bai, Z.; Scheibe, B.; Beck, N.; Long, B. N.; Justiniano, S.; Albrecht-Schönzart, T. E.; Celis-Barros, C. Isolation of a Californium(II) Crown–Ether Complex. *Nat. Chem.* **2023**, *15* (5), 722–728.
- (19) Sokolova, M. N.; Fedossev, A. M.; Andreev, G. B.; Budantseva, N. A.; Yusov, A. B.; Moisy, P. Synthesis and Structural Examination of Complexes of Am(IV) and Other Tetravalent Actinides with Lacunary Heteropolyanion A₂P₂W₁₇O₆₁–. *Inorg. Chem.* **2009**, *48* (19), 9185–9190.
- (20) Silver, M. A.; Cary, S. K.; Garza, A. J.; Baumbach, R. E.; Arico, A. A.; Galmin, G. A.; Chen, K.-W.; Johnson, J. A.; Wang, J. C.; Clark, R. J.; Chemey, A.; Eaton, T. M.; Marsh, M. L.; Seidler, K.; Galley, S. S.; van de Burgt, L.; Gray, A. L.; Hobart, D. E.; Hanson, K.; Van Cleve, S. M.; Gendron, F.; Autschbach, J.; Scuseria, G. E.; Maron, L.; Speldrich, M.; Kögerler, P.; Celis-Barros, C.; Páez-Hernández, D.; Arratia-Pérez, R.; Ruf, M.; Albrecht-Schmitt, T. E. Electronic Structure and Properties of Berkelium Iodates. *J. Am. Chem. Soc.* **2017**, *139* (38), 13361–13375.
- (21) Zhang, H.; Li, A.; Li, K.; Wang, Z.; Xu, X.; Wang, Y.; Sheridan, M. V.; Hu, H.-S.; Xu, C.; Alekseev, E. V.; Zhang, Z.; Yan, P.; Cao, K.; Chai, Z.; Albrecht-Schönzart, T. E.; Wang, S. Ultrafiltration Separation of Am(VI)-Polyoxometalate from Lanthanides. *Nature* **2023**, *616* (7957), 482–487.
- (22) Sperling, J. M.; Warzecha, E. J.; Celis-Barros, C.; Sergentu, D.-C.; Wang, X.; Klamm, B. E.; Windorff, C. J.; Gaiser, A. N.; White, F. D.; Beery, D. A.; Chemey, A. T.; Whitefoot, M. A.; Long, B. N.; Hanson, K.; Kögerler, P.; Speldrich, M.; Zurek, E.; Autschbach, J.; Albrecht-Schönzart, T. E. Compression of Curium Pyrrolidine-Dithiocarbamate Enhances Covalency. *Nature* **2020**, *583* (7816), 396–399.
- (23) Long, B. N.; Sperling, J. M.; Windorff, C. J.; Albrecht-Schönzart, T. E. Characterization of the Organoamericium Complex Cp'3Am. *Organometallics* **2023**, *42* (21), 3048–3052.
- (24) Long, B. N.; Beltrán-Leiva, M. J.; Sperling, J. M.; Poe, T. N.; Celis-Barros, C.; Albrecht-Schönzart, T. E. Altering the Spectroscopy, Electronic Structure, and Bonding of Organometallic Curium(III) upon Coordination of 4,4'-bipyridine. *Nat. Commun.* **2023**, *14* (1), 3774.
- (25) Cary, S. K.; Silver, M. A.; Liu, G.; Wang, J. C.; Bogart, J. A.; Stritzinger, J. T.; Arico, A. A.; Hanson, K.; Schelter, E. J.; Albrecht-Schmitt, T. E. Spontaneous Partitioning of Californium from Curium: Curious Cases from the Crystallization of Curium Coordination Complexes. *Inorg. Chem.* **2015**, *54* (23), 11399–11404.
- (26) Arteaga, A.; Nicholas, A. D.; Ducati, L. C.; Autschbach, J.; Surbella, R. G. I. Americium Oxalate: An Experimental and Computational Investigation of Metal–Ligand Bonding. *Inorg. Chem.* **2023**, *62* (12), 4814–4822.
- (27) Arteaga, A.; Nicholas, A. D.; Sinnwell, M. A.; McNamara, B. K.; Buck, E. C.; Surbella, R. G. I. Expanding the Transuranic Metal–Organic Framework Portfolio: The Optical Properties of Americium(III) MOF-76. *Inorg. Chem.* **2023**, *62*, 21036.
- (28) Colliard, I.; Lee, J. R. I.; Colla, C. A.; Mason, H. E.; Sawvel, A. M.; Zavarin, M.; Nyman, M.; Deblonde, G. J.-P. Polyoxometalates as Ligands to Synthesize, Isolate and Characterize Compounds of Rare Isotopes on the Microgram Scale. *Nat. Chem.* **2022**, *14* (12), 1357–1366.
- (29) Colliard, I.; Deblonde, G. J.-P. Polyoxometalate Ligands Reveal Different Coordination Chemistries Among Lanthanides and Heavy Actinides. *JACS Au* **2024**, *4* (7), 2503–2513.
- (30) Colliard, I.; Deblonde, G. J.-P. Characterization of the First Peacock–Weakley Polyoxometalate Containing a Transplutonium Element: Curium Bis-Pentatungstate [Cm(W₅O₁₈)₂]⁹⁻. *Chem. Commun.* **2024**, *60* (47), 5999–6002.
- (31) Tézé, A.; Michelon, M.; Hervé, G. Syntheses and Structures of the Tungstoborate Anions. *Inorg. Chem.* **1997**, *36* (4), 505–509.
- (32) Keggin, J. F. The Structure and Formula of 12-Phosphotungstic Acid. *Proceedings of the Royal Society of London. Series A, Containing Papers of a Mathematical and Physical Character* **1934**, *144* (851), 75–100.
- (33) Pope, M. T. *Heteropoly and Isopoly Oxometalates*, 1st ed.; Inorganic Chemistry Concepts; Springer: Berlin, Heidelberg, 1983.

- (34) Colliard, I.; Deblonde, G. J.-P. From + I to + IV, Alkalides to Actinides: Capturing Cations across the Periodic Table with Keggin Polyoxometalate Ligands. *Inorg. Chem.* **2024**, *63* (35), 16293–16303.
- (35) Nielsen, V. R. M.; Le Guennic, B.; Sørensen, T. J. Evaluation of Point Group Symmetry in Lanthanide(III) Complexes: A New Implementation of a Continuous Symmetry Operation Measure with Autonomous Assignment of the Principal Axis. *J. Phys. Chem. A* **2024**, *128* (28), 5740–5751.
- (36) Misra, A.; Kozma, K.; Streb, C.; Nyman, M. Beyond Charge Balance: Counter-Cations in Polyoxometalate Chemistry. *Angew. Chem., Int. Ed.* **2020**, *59* (2), 596–612.
- (37) Kaledin, A. L.; Yin, Q.; Hill, C. L.; Lian, T.; Musaev, D. G. Ion-Pairing in Polyoxometalate Chemistry: Impact of Fully Hydrated Alkali Metal Cations on Properties of the Keggin [PW₁₂O₄₀]³⁻ Anion. *Dalton Trans.* **2020**, *49* (32), 11170–11178.
- (38) Bünzli, J.-C. G.; Piguet, C. Taking Advantage of Luminescent Lanthanide Ions. *Chem. Soc. Rev.* **2005**, *34* (12), 1048–1077.
- (39) Storm Thomsen, M.; Anker, A. S.; Kacenauskaite, L.; Sørensen, T. J. We Are Never Ever Getting (Back to) Ideal Symmetry: Structure and Luminescence in a Ten-Coordinated Europium(III) Sulfate Crystal. *Dalton Trans.* **2022**, *51* (23), 8960–8963.
- (40) Kofod, N.; Storm Thomsen, M.; Nawrocki, P.; Sørensen, T. J. Revisiting the Assignment of Innocent and Non-Innocent Counterions in Lanthanide(III) Solution Chemistry. *Dalton Trans.* **2022**, *51* (20), 7936–7949.
- (41) Thomsen, M. S.; Nawrocki, P. R.; Kofod, N.; Sørensen, T. J. Seven Europium(III) Complexes in Solution – The Importance of Reporting Data When Investigating Luminescence Spectra and Electronic Structure. *Eur. J. Inorg. Chem.* **2022**, *2022* (27), No. e202200334.
- (42) Neves, C. S.; Granadeiro, C. M.; Cunha-Silva, L.; Ananias, D.; Gago, S.; Feio, G.; Carvalho, P. A.; Eaton, P.; Balula, S. S.; Pereira, E. Europium Polyoxometalates Encapsulated in Silica Nanoparticles – Characterization and Photoluminescence Studies. *Eur. J. Inorg. Chem.* **2013**, *2013* (16), 2877–2886.
- (43) Jing, J.-X.; Shi, N.; Sun, Y.-Q.; Li, X.-X.; Zheng, S.-T. An Inorganic-Organic Hybrid Polyoxotungstogermanate Based on [Ln(α -GeW₁₁O₃₉)₂] Dimer and Dimethylammonium: Synthesis, Crystal Structure and Photoluminescence Property. *J. Mol. Struct.* **2022**, *1250*, No. 131686.
- (44) Nielsen, V. R. M.; Nawrocki, P. R.; Sørensen, T. J. Electronic Structure of Neodymium(III) and Europium(III) Resolved in Solution Using High-Resolution Optical Spectroscopy and Population Analysis. *J. Phys. Chem. A* **2023**, *127* (16), 3577–3590.
- (45) Storm Thomsen, M.; Andersen, H. O. B.; Sørensen, T. J. Long Story Short: Donor Set Symmetry in [Eu(DOTA)(H₂O)]⁻ Crystals Determines the Electronic Structure. *Dalton Trans.* **2022**, *51* (37), 14118–14124.
- (46) Boubals, N.; Wagner, C.; Dumas, T.; Chanéac, L.; Manie, G.; Kaufholz, P.; Marie, C.; Panak, P. J.; Modolo, G.; Geist, A.; Guilbaud, P. Complexation of Actinide(III) and Lanthanide(III) with H₄TPAEN for a Separation of Americium from Curium and Lanthanides. *Inorg. Chem.* **2017**, *56* (14), 7861–7869.
- (47) Deblonde, G. J.-P.; Mattocks, J. A.; Wang, H.; Gale, E. M.; Kersting, A. B.; Zavarin, M.; Cotruvo, J. A. Characterization of Americium and Curium Complexes with the Protein Lanmodulin: A Potential Macromolecular Mechanism for Actinide Mobility in the Environment. *J. Am. Chem. Soc.* **2021**, *143* (38), 15769–15783.
- (48) Bauer, N.; Panak, P. J. Influence of Carbonate on the Complexation of Cm(III) with Human Serum Transferrin Studied by Time-Resolved Laser Fluorescence Spectroscopy (TRLFS). *New J. Chem.* **2015**, *39* (2), 1375–1381.
- (49) Moll, H.; Glorius, M.; Bernhard, G. Curium(III) Complexation with Desferrioxamine B (DFO) Investigated Using Fluorescence Spectroscopy. *BCSJ* **2008**, *81* (7), 857–862.
- (50) Skerencák-Frech, A.; Trumm, M.; Fröhlich, D. R.; Panak, P. J. Coordination and Thermodynamics of Trivalent Curium with Malonate at Increased Temperatures: A Spectroscopic and Quantum Chemical Study. *Inorg. Chem.* **2017**, *56* (17), 10172–10180.
- (51) Leguay, S.; Vercouter, T.; Topin, S.; Aupiais, J.; Guillaumont, D.; Miguirditchian, M.; Moisy, P.; Le Naour, C. New Insights into Formation of Trivalent Actinides Complexes with DTPA. *Inorg. Chem.* **2012**, *51* (23), 12638–12649.
- (52) Thouvenot, P.; Hubert, S.; Edelstein, N. Spectroscopic Study and Crystal-Field Analysis of Cm³⁺ in the Cubic-Symmetry Site of ThO₂. *Phys. Rev. B* **1994**, *50* (14), 9715–9720.
- (53) Liu, G. K.; Zhorin, V. V.; Li, S. T.; Beitz, J. V. Crystal Field Analysis and Monte Carlo Simulation of Lattice Disordering for Cm³⁺ in YPO₄ and LuPO₄. *J. Chem. Phys.* **2000**, *112* (1), 373–382.
- (54) Kimura, T.; Nagaishi, R.; Kato, Y.; Yoshida, Z. Luminescence Study on Solvation of Americium(III), Curium(III) and Several Lanthanide(III) Ions in Nonaqueous and Binary Mixed Solvents. *Radiochim. Acta* **2001**, *89* (3), 125–130.
- (55) Sheldrick, G. M. Bruker-Siemens Area Detection Absorption Other Correction, SADABS 2008.
- (56) Sheldrick, G. M. SHELLXT – Integrated Space-Group and Crystal-Structure Determination. *Acta Cryst. A* **2015**, *71* (1), 3–8.
- (57) Dolomanov, O. V.; Bourhis, L. J.; Gildea, R. J.; Howard, J. a. K.; Puschmann, H. OLEX2: A Complete Structure Solution, Refinement and Analysis Program. *J. Appl. Crystallogr.* **2009**, *42* (2), 339–341.